

Spin Hall effect in the  $\alpha$  and  $\beta$  phases of  $\text{Ta}_x\text{W}_{1-x}$  alloysLijuan Qian<sup>1</sup>, Kang Wang<sup>1</sup>, Yi Zheng<sup>2</sup>, and Gang Xiao<sup>1,\*</sup><sup>1</sup>*Department of Physics, Brown University, Providence, Rhode Island 02912, USA*<sup>2</sup>*Department of Mechanical and Industrial Engineering, Northeastern University, Boston, Massachusetts 02115, USA* (Received 26 May 2020; revised 12 September 2020; accepted 14 September 2020; published 28 September 2020)

$\beta$ -W and  $\beta$ -Ta are well known for their large spin Hall angles (SHAs), while  $\alpha$ -W and  $\alpha$ -Ta possess small SHAs. Recent theoretical studies predicted that alloying Ta with W could enhance the SHA. In this work, a systematic study is performed on the spin Hall effect (SHE) in  $\text{Ta}_x\text{W}_{1-x}$  alloys in the full composition range from  $x = 0$  to 1. We have obtained the structural phase diagram and SHAs of the  $\alpha$ - and  $\beta$ - $\text{Ta}_x\text{W}_{1-x}$  alloy system, based on x-ray-diffraction, transmission electron microscopy, magnetotransport measurement, and macrospin model analysis. We have observed large SHAs ranging from  $-0.06$  to  $-0.23$  in  $\alpha$ - $\text{Ta}_x\text{W}_{1-x}$  and a maximum SHA of  $-0.59$  in 5.3-nm-thick  $\beta$ - $\text{Ta}_x\text{W}_{1-x}$ . In addition, a linear correlation between SHA and resistivity in  $\text{Ta}_x\text{W}_{1-x}$  has been uncovered, providing evidence that the SHE in  $\text{Ta}_x\text{W}_{1-x}$  is caused by the intrinsic mechanism and/or side-jump scattering. Furthermore, we have observed an unconventional thickness dependence of SHA in  $\beta$ - $\text{Ta}_{0.25}\text{W}_{0.75}$ , which peaks at 5.3 nm. The decay of SHA upon increasing thickness is likely to be caused by the  $\beta$ - to  $\alpha$ -phase transition.

DOI: [10.1103/PhysRevB.102.094438](https://doi.org/10.1103/PhysRevB.102.094438)

## I. INTRODUCTION

Recent research has demonstrated that spin current induced spin-transfer torque can manipulate the magnetization in both ferromagnetic (FM) [1–4] and antiferromagnetic (AFM) [5–7] solids. This property has enabled the development of ultrafast and energy-efficient spintronics such as magnetic random access memory and spin-logic devices [8–12]. Spin Hall effect (SHE) [13,14], which converts charge current into spin current through spin-orbit coupling, is one of the most effective means of generating pure spin current. The generated spin current is given by  $\mathbf{J}_s = (\hbar/2e)\Theta_{\text{SH}}(\boldsymbol{\sigma} \times \mathbf{J}_c)$ , where  $\mathbf{J}_c$  is the charge current density,  $\mathbf{J}_s$  is the generated spin current density,  $\boldsymbol{\sigma}$  is the spin polarization unit vector,  $\hbar$  is the reduced Plank constant,  $e$  is the elementary charge,  $\Theta_{\text{SH}}$  is the spin Hall angle (SHA) characterizing the conversion efficiency [14,15]. Large SHAs have been reported in heavy metals with strong spin-orbit coupling, such as Pt [3,16,17],  $\beta$ -W [15,18], and  $\beta$ -Ta [1,19]. To date, the highest SHA reported at room temperature in metals is  $-0.65$  in thick  $\beta$ -W films [20]. In addition to pure metals, recent studies revealed that alloying is an effective method for tuning the SHA and the resistivity of solids [21,22]. Most efforts so far have been focused on alloys of solids with small SHAs (e.g., Au and Cu) and heavy metals with large SHAs (e.g., Ta and Pt) [23–28]. The prospect of acquiring an enhanced SHA through alloying is not only attractive for applications, but also interesting fundamentally in understanding the basic mechanisms of the SHE versus the electronic structure of alloyed solids.

In this work, we perform a systematic study of the SHE by alloying two heavy elements: Ta and W. Both are well known for their characteristically large SHAs in the  $\beta$  phase

and small SHAs in the  $\alpha$  phase. In spite of similar crystalline structures [29,30], the SHA of  $\beta$ -W [20] is three times larger than that of  $\beta$ -Ta [31]. Ta-W alloys provide us with a good platform to understand the major difference between  $\beta$ -Ta and  $\beta$ -W. Besides, recent theoretical studies have predicted an enhancement in the intrinsic SHE in Ta-W alloys. Sui *et al.* [32] performed first-principles calculations to show that the spin Hall conductivity (SHC)  $\sigma_{\text{SH}} = \frac{\hbar}{2e} \frac{\Theta_{\text{SH}}}{\rho_{xx}}$ , where  $\rho_{xx}$  is the longitudinal resistivity, of both  $\alpha$ -W and  $\beta$ -W can be enhanced when alloyed with Ta. They predicted the  $\sigma_{\text{SH}} = -3546(\hbar/2e)$  (S/cm) in  $\beta$ - $\text{Ta}_{0.125}\text{W}_{0.875}$  with a SHA of  $-0.5$ . Separately, Derunova *et al.* [33] predicted an even larger  $\sigma_{\text{SH}} = -4500(\hbar/2e)$  (S/cm).

We have investigated the SHE of both  $\alpha$ - $\text{Ta}_x\text{W}_{1-x}$  and  $\beta$ - $\text{Ta}_x\text{W}_{1-x}$  alloy thin films in the full composition range of  $x = 0$  to 1, and at various thicknesses ( $t$ ). We have measured the effective SHA,  $\Theta_{\text{SH}}^{\text{eff}} = \Theta_{\text{SH}}T_{\text{int}}$ , where  $T_{\text{int}}$  is the interfacial spin transparency [16] between the  $\text{Ta}_x\text{W}_{1-x}$  layer and the adjacent FM layer. The value of  $\Theta_{\text{SH}}^{\text{eff}}$  yields a lower bound of the SHA in a  $\text{Ta}_x\text{W}_{1-x}$  film. We have obtained large  $\Theta_{\text{SH}}^{\text{eff}}$  ranging from  $-0.06$  to  $-0.23$  in  $\alpha$ - $\text{Ta}_x\text{W}_{1-x}$ , corresponding to the SHC from  $-338$  to  $-1259(\hbar/2e)$ (S/cm). In  $\beta$ - $\text{Ta}_x\text{W}_{1-x}$ , the  $\Theta_{\text{SH}}^{\text{eff}}$  is in the range of  $-0.26$  to  $-0.59$ , corresponding to the SHC from  $-1059$  to  $-1842(\hbar/2e)$  (S/cm). The largest  $\Theta_{\text{SH}}^{\text{eff}} = -0.59 \pm 0.04$ , corresponding to the SHC of  $-1842(\hbar/2e)$  (S/cm), is achieved in the 5.3-nm-thick  $\text{Ta}_{0.25}\text{W}_{0.75}$ . This value is much larger than the SHA in  $\beta$ -Ta and  $\beta$ -W of similar thickness and is comparable to the largest SHA reported in heavy metals [20,27]. We have also studied the thickness dependence of  $\Theta_{\text{SH}}^{\text{eff}}$  in  $\text{Ta}_{0.25}\text{W}_{0.75}$ .  $\Theta_{\text{SH}}^{\text{eff}}$  peaks at 5.3 nm and decreases as the thickness is further increased, which is probably due to the phase transition from the  $\beta$  to the  $\alpha$  phase. From the dependence of  $\Theta_{\text{SH}}^{\text{eff}}$  on resistivity, we have found that the intrinsic mechanism and/or side jump scattering contribute to the SHE when the

\*Gang\_Xiao@brown.edu

resistivity  $\rho_{xx}$  is below  $250 \mu\Omega \text{ cm}$ . When  $\rho_{xx} > 250 \mu\Omega \text{ cm}$ , the intrinsic SHE is suppressed due to small grain sizes in the thin films.

## II. SAMPLE FABRICATION

We used a home-made high vacuum magnetron sputtering system to prepare a series of  $\text{Ta}_x\text{W}_{1-x}$  thin films with Ta concentration  $x = 0, 0.1, 0.25, 0.5, 0.75, 0.9$ , and  $1$ . The designed thicknesses of each composition are 10 and 15 nm. The real thickness of each sample was measured by x-ray reflectivity (XRR). For  $x = 0.25$ , we also fabricated a series of samples with varying thicknesses from 3.0 to 28.5 nm. Each sample has the following layer sequence: substrate/ $\text{Ta}_x\text{W}_{1-x}(t)$ / $\text{Co}_{40}\text{Fe}_{40}\text{B}_{20}(1.0)$ / $\text{MgO}(1.6)$ / $\text{Ta}(1.3)$  (the number in parentheses refers to the thickness of the corresponding layer in nm). The substrates are thermally oxidized silicon wafers.

For a given  $\text{Ta}_x\text{W}_{1-x}$ , we codeposited the sample from pure Ta and W targets with the base vacuum pressure of  $1.0 \times 10^{-7}$  Torr. During deposition, we rotated the substrate continuously at the rate of 6.1 rpm over the Ta and W targets. The composition of an alloy is controlled by the relative sputtering yields of Ta and W, well calibrated to the powers applied to the two targets. The net deposition rate is about  $1.0 \text{ \AA}$  per rotation. The other layers ( $\text{Co}_{40}\text{Fe}_{40}\text{B}_{20}$ , MgO, and Ta) were directly sputtered from each corresponding target. The 1.0-nm-thick  $\text{Co}_{40}\text{Fe}_{40}\text{B}_{20}$  layer is the FM layer exhibiting perpendicular magnetic anisotropy (PMA). The PMA was achieved after annealing samples at a proper temperature in a 0.4-T out-of-plane magnetic field. The annealing temperatures are  $200^\circ\text{C}$  and  $280^\circ\text{C}$  for  $x \geq 0.5$  and  $x < 0.5$ , respectively. The MgO layer is required for the onset of PMA in  $\text{Co}_{40}\text{Fe}_{40}\text{B}_{20}$  [34,35], and the 1.3-nm-thick Ta is the capping layer. We patterned thin films into standard Hall bars with the dimension of  $20 \mu\text{m} \times 55 \mu\text{m}$  by using photolithography and physical ion milling, for the purpose of measuring both the transverse Hall resistivity and longitudinal resistivity.

## III. CRYSTALLINE STRUCTURE

It is well known that both Ta and W have two types of crystalline structures [29,30,36,37]: the body-centered-cubic (bcc) structure known as the  $\alpha$  phase and the A15 structure known as the  $\beta$  phase. We performed the x-ray-diffraction (XRD) measurement using the Bruker D8 Discover XRD system to determine the crystalline structures of  $\text{Ta}_x\text{W}_{1-x}$  thin films. Figures 1(a)–1(c) show the XRD patterns of a few representative films in  $\beta$ -phase and  $\alpha$ -phase alloys. As shown in Fig. 1(a), pure W films (with thicknesses of 8.9 and 19.1 nm) and  $\text{Ta}_{0.1}\text{W}_{0.9}$  show two peaks corresponding to the characteristic (200) and (210) peaks of the  $\beta$ -phase structure. In Figs. 1(b) and 1(c), one strong peak corresponding to the (110) peak of the  $\alpha$ -phase structure is observed. Figure 1(b) shows that more Ta-concentrated alloy films,  $\text{Ta}_{0.25}\text{W}_{0.75}$ ,  $\text{Ta}_{0.5}\text{W}_{0.5}$ , and  $\text{Ta}_{0.75}\text{W}_{0.25}$ , with a thickness of about 10 nm, are in the  $\alpha$  phase. Figure 1(c) shows that  $\text{Ta}_{0.25}\text{W}_{0.75}$  films with thicknesses between 9.0 and 28.5 nm also form  $\alpha$ -phase alloys. Using Bragg's law, we calculated the lattice constant of the  $\alpha$ - $\text{Ta}_x\text{W}_{1-x}$  bcc structure from the peak positions, as

plotted in Fig. 1(d). The data of the bulk  $\alpha$ -Ta and  $\alpha$ -W are from the ICDD's Powder Diffraction File database [38]. Figure 1(d) shows that the lattice constant increases monotonically with the Ta composition for  $\alpha$ - $\text{Ta}_x\text{W}_{1-x}$ . Using the Scherrer equation  $d = \frac{K\lambda}{\text{FWHM} \sin\theta}$ , where  $\lambda$  is the x-ray wavelength, FWHM is the full width at half maximum of the peak,  $\theta$  is the Bragg angle,  $K$  is a shape factor which is mostly estimated as 0.9 [29,39], we can estimate the crystallite dimension of the samples. This dimension is determined by the smaller value of the grain size and sample thickness [40]. Figure 1(e) shows that the estimated crystallite dimension of each sample is between 8% and 70% of its film thickness. Therefore, the Scherrer equation provides a good estimate of grain sizes of the samples. A general observation from Fig. 1(e) reveals that the thicker the film and the lower the Ta concentration, the larger the grain size.

Crystalline grain boundaries are effective electron scattering centers, increasing the extrinsic resistivity of a thin film. In Fig. 1(f), we presented the relation between resistivities of  $\text{Ta}_x\text{W}_{1-x}$  thin films versus the inverse of the thin films' grain sizes,  $1/d$ . The linear scaling between the resistivity and  $1/d$  is an indication that the grain-boundary scattering is the dominant source of resistivity and the grain size sets the scale for the electron mean-free path [41,42]. Overall, the resistivity of  $\text{Ta}_x\text{W}_{1-x}$  ranges broadly from 60 to  $360 \mu\Omega \text{ cm}$ . Although for bulk Ta and W,  $\alpha$ -phase samples typically have lower resistivity than  $\beta$ -phase samples [18,20,30,36], in our samples,  $\alpha$ -phase films can have resistivities as large as that in  $\beta$ -phase films ( $> 150 \mu\Omega \text{ cm}$ ). The higher resistivity in our samples compared with bulk Ta and W is because of small grain sizes of samples, as well as the potential partial oxidation of thin films due to the low deposition rate during sputtering.

## IV. SPIN HALL ANGLE

To obtain effective spin Hall angles ( $\Theta_{\text{SH}}^{\text{eff}}$ ) of alloys, we measured the magnetization response to the spin current when applying an external magnetic field  $\mathbf{B}_{\text{ext}} = B_{\text{ext}}\hat{y}$  along the longitudinal direction of the Hall bar ( $y$  axis), as illustrated in Fig. 2(a). We analyzed the measurement results through a macrospin model [3,19].  $\mathbf{B}_{\text{ext}}$  forces the magnetization vector  $\mathbf{M}$  in the perpendicularly magnetized  $\text{Co}_{40}\text{Fe}_{40}\text{B}_{20}$  layer to tilt ( $\theta < 90^\circ$ ). Increasing  $B_{\text{ext}}$  leads the magnetization to rotate coherently towards the  $y$  axis. The orientation angle  $\theta$  of the magnetization vector  $\hat{m}$  can be determined by the equilibrium condition of three torques in Eq. (1).

$$\begin{aligned} \tau_{\text{tot}} &\equiv \hat{x}(\tau_{\text{ST}} + \tau_{\text{ext}} + \tau_{\text{an}}) \\ &= \tau_{\text{ST}}^0 + B_{\text{ext}} \sin(\theta - \delta) - B_{\text{an}}^0 \sin\theta \cos\theta = 0. \end{aligned} \quad (1)$$

$\tau_{\text{ST}} = \tau_{\text{ST}}^0[\hat{m} \times (\hat{\sigma} \times \hat{m})]$  is the spin-transfer torque from the spin current,  $\tau_{\text{ext}} = -\hat{m} \times \mathbf{B}_{\text{ext}} = B_{\text{ext}} \sin(\theta - \delta)\hat{x}$  is the spin torque from the external magnetic field, where  $\delta$  is a small yet unavoidable misalignment angle of  $\mathbf{B}_{\text{ext}}$  relative to the  $y$  axis, which is typically between  $-5^\circ$  and  $5^\circ$ .  $\tau_{\text{an}} = -\hat{m} \times \mathbf{B}_{\text{an}} = -B_{\text{an}}^0 \sin\theta \cos\theta \hat{x}$  is the spin torque from the anisotropy. In this model, we only take into considerations spin torques along the  $x$  axis. This is reasonable because the magnetization remains in the  $y$ - $z$  plane with the application of a large  $\mathbf{B}_{\text{ext}}$ . The

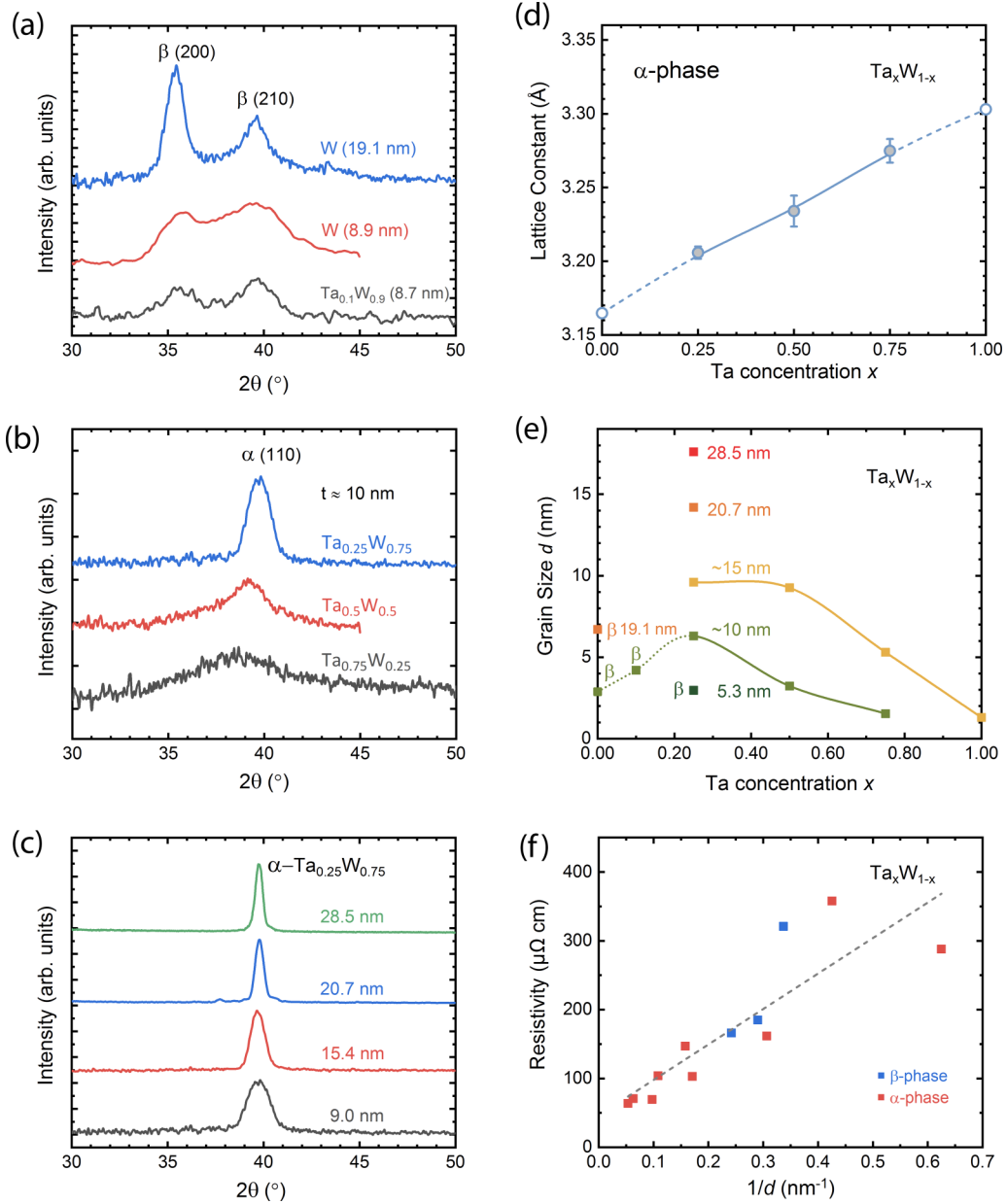


FIG. 1. (a)–(c) X-ray-diffraction patterns of  $\text{Ta}_x\text{W}_{1-x}$  thin films in either  $\alpha$  or  $\beta$  phase at different thicknesses. (d) Lattice constants of bcc structured  $\alpha$ -phase  $\text{Ta}_x\text{W}_{1-x}$  with various composition. (e) Grain size ( $d$ ) in thin films with various compositions and thicknesses. The grain size of the 5.3-nm-thick  $\beta\text{-Ta}_{0.25}\text{W}_{0.75}$  is derived from the TEM image because it's too thin to be measured by XRD, while others are derived from the XRD measurements. (f) Resistivity of a thin film vs the inverse of the grain size ( $1/d$ ).

external magnetic field is much larger than the Oersted field along the  $x$  axis, generated by the charge current flowing along the  $y$  axis. We sent DC currents with current density  $J_c$  along the  $+y$  and  $-y$  directions respectively when applying different values of  $B_{\text{ext}}$ . The spin-transfer torque  $\tau_{\text{ST}}^0$  can then be determined from the response of  $\theta$  to  $B_{\text{ext}}$  as shown in Eq. (2) which is derived from Eq. (1) [19],

$$\tau_{\text{ST}}^0 = \frac{J_s}{M_s t_{\text{FM}}} = -\frac{1}{2} [B_{\text{ext}+}(\theta) - B_{\text{ext}-}(\theta)] \sin(\theta - \delta). \quad (2)$$

$B_{\text{ext}+}(\theta)$  and  $B_{\text{ext}-}(\theta)$  are the external magnetic fields at which the magnetization is tilted at the angle  $\theta$  while the sample is subjected to a positive ( $+y$  axis) and a negative ( $-y$  axis)

charge current, respectively [inset in Fig. 2(d)].  $M_s$  is the saturation magnetization.  $t_{\text{FM}}$  is the FM layer thickness.  $J_s$  is the spin current density. The sign of  $J_s$  represents the spin polarization directions. The value of  $\Theta_{\text{SH}}^{\text{eff}} = (\frac{2e}{\hbar})J_s/J_c$  can then be easily calculated from Eq. (2).

We use the measurement on a 5.3-nm-thick  $\beta\text{-Ta}_{0.25}\text{W}_{0.75}$  film as an example. Figure 2(b) shows the hysteresis loop of the anomalous Hall resistance,  $R_{\text{H}}$ , as a function of a perpendicular magnetic field  $B_z$ . The value of  $R_{\text{H}}$  can be used to sense the  $z$  component  $M_z$  (or  $\theta$ ) of the magnetization. The perfect square loop indicates the robust PMA of the 1.0-nm-thick  $\text{Co}_{40}\text{Fe}_{40}\text{B}_{20}$  overlayer, with the coercivity of 4.1 mT. Figure 2(c) shows the in-plane magnetization

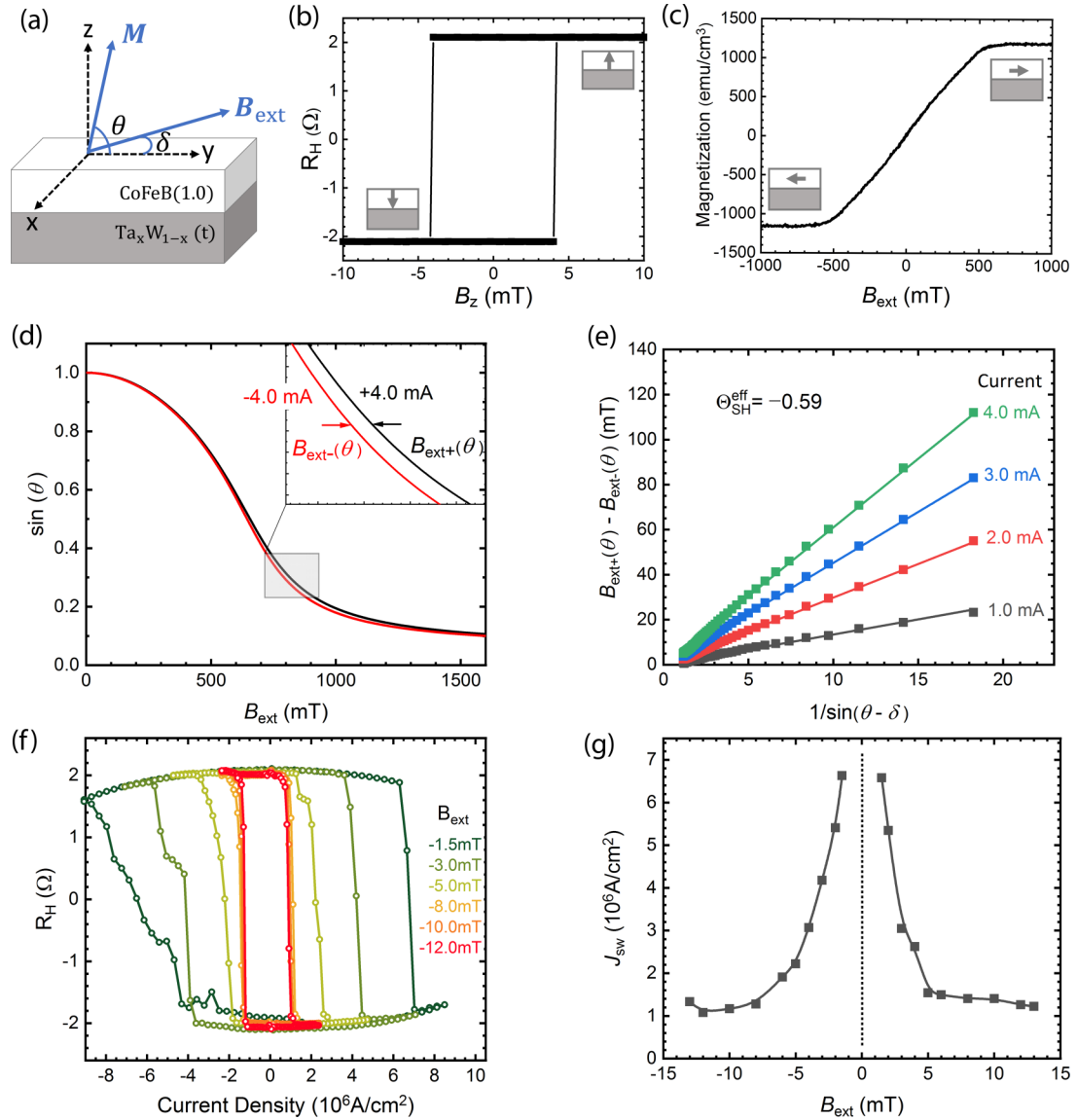


FIG. 2. (a) Schematic of a thin-film sample with magnetization ( $M$ ) at an external magnetic field ( $B_{\text{ext}}$ ) for the measurement of SHA based on the macrospin model. All measurements in Fig. 2 were performed on a 5.3-nm-thick  $\text{Ta}_{0.25}\text{W}_{0.75}$  thin film. (b) Hysteresis loop of anomalous Hall resistance in an out-of-plane magnetic field ( $B_z$ ). (c) In-plane magnetization as a function of an in-plane magnetic field. (d) Dependence of magnetization angle ( $\theta$ ) on  $B_{\text{ext}}$  when sending a charge current of  $\pm 4.0$  mA. (e) Linear fittings of  $[B_{\text{ext}+}(\theta) - B_{\text{ext}-}(\theta)]$  vs  $1/\sin(\theta - \delta)$  at various charge currents, leading to the determination of SHA  $\Theta_{\text{SH}}^{\text{eff}} = -0.59$ . (f) Hall resistance vs current density when an external magnetic field from  $-1.5$  mT to  $-12.0$  mT is applied. (g) Critical switching current density  $J_{\text{sw}}$  in the  $\text{Ta}_{0.25}\text{W}_{0.75}$  layer when applying different external magnetic field  $B_{\text{ext}}$ .

curve of the  $\text{Co}_{40}\text{Fe}_{40}\text{B}_{20}$  layer, measured using the Quantum Design<sup>®</sup> Physical Property Measurement System. The saturation field is about 50 mT and the saturation magnetization  $M_s$  is  $1239 \text{ emu/cm}^3$  which is consistent with previous measurement results on  $\text{Co}_{40}\text{Fe}_{40}\text{B}_{20}$  [18,43]. In Fig. 2(d), we show  $\sin(\theta)$  as a function of  $B_{\text{ext}}$  when sending the charge currents of  $\pm 4.0$  mA. At a given  $\theta$  from  $0^\circ$  to  $90^\circ$ , we can extract the value of  $B_{\text{ext}+}(\theta) - B_{\text{ext}-}(\theta)$ . According to Eq. (2),  $B_{\text{ext}+}(\theta) - B_{\text{ext}-}(\theta)$  is linearly dependent on  $1/\sin(\theta - \delta)$  with a slope  $-2\tau_{\text{ST}}^0$ . The results of  $B_{\text{ext}+}(\theta) - B_{\text{ext}-}(\theta)$  versus  $1/\sin(\theta - \delta)$  when sending various charge currents through the sample ( $\delta$  is determined to be  $2^\circ$  through fitting) are presented in Fig. 2(e). Using Eq. (2), we determined that  $\Theta_{\text{SH}}^{\text{eff}} =$

$-0.59$  for the 5.3-nm-thick  $\beta\text{-Ta}_{0.25}\text{W}_{0.75}$  film, carrying the same negative sign as pure  $\beta\text{-Ta}$  and  $\beta\text{-W}$ . This value is among the largest SHAs reported so far in non-FM metals at room temperature [20,23,27].

Such a large SHA is expected to enable effective switching of magnetization from spin up to spin down (or vice versa) with a relatively small critical charge current density  $J_{\text{sw}}$ . We measured the current induced magnetization switching in this sample when applying an in-plane magnetic field from 1.5 to 12.0 mT. Figure 2(f) shows the Hall resistance  $R_H$  versus charge current density in the  $\text{Ta}_x\text{W}_{1-x}$  layer in the sample. Figure 2(g) shows the results of  $J_{\text{sw}}$  versus the in-plane external magnetic field. The switching current

decreases with the increasing magnetic field as expected since the energy barrier for switching is lowered by the in-plane magnetic field. When the in-plane magnetic field increases from 1.5 to 5.0 mT,  $J_{sw}$  decreases rapidly and reaches about  $1.2 \times 10^6 \text{ A/cm}^2$ . This is among the lowest switching current density reported [18]. When the field goes beyond 5.0 mT, the switching current decreases slowly with increasing magnetic field. Similar behavior has also been observed in previous research [4,44]. A possible explanation of such behavior is the combined effect of the different current densities required for the nucleation and domain propagation processes. The magnetization switching starts with the nucleation of reversed magnetic domains and is followed by a domain propagation process [45–47]. The domain nucleation generally occurs at the edge of samples where the perpendicular anisotropy is lower such that the energy barrier for magnetization switching is lower. The critical current for domain nucleation is expected to decrease when the in-plane magnetic field is increased, which governs the curve in the low-field region in Fig. 2(g). When the in-plane magnetic field is large ( $>5.0$  mT in our sample), the current required for domain nucleation is rather low. In this case, the critical current for magnetization switching is governed by the critical current for domain propagation. The critical current for domain propagation is almost independent on the in-plane magnetic field strength, which has been previously reported [48].

Due to its small thickness, XRD cannot generate a sufficient signal for us to determine the structure of the 5.3-nm-thick  $\text{Ta}_{0.25}\text{W}_{0.75}$ . Instead, we used transmission electron microscopy (TEM) for structural investigation of this sample. Figure 3(a) shows the TEM micrograph, which reveals the polycrystalline morphology. Through the fast Fourier image analysis, we obtain that the average atomic spacing is  $2.252 \pm 0.024 \text{ \AA}$ , which is close to the spacing ( $2.2584 \text{ \AA}$ ) of the (210) plane of  $\beta$ -W [38]. This is strong evidence of the  $\beta$ -phase structure in this particular thin film.

Figure 3(b) presents the resistivity data for  $\text{Ta}_{0.25}\text{W}_{0.75}$  thin films with various thicknesses from 3.0 to 28.5 nm. The  $\beta$ -phase  $\text{Ta}_{0.25}\text{W}_{0.75}$  with thicknesses in the range of 3.0 to 7.5 nm all exhibit very high resistivities ( $>270 \mu\Omega \text{ cm}$ ). Thicker  $\text{Ta}_{0.25}\text{W}_{0.75}$  films with thicknesses in the 9.0–28.5-nm range, all in  $\alpha$  phase [Fig. 1(c)], have significantly lower resistivities ( $<150 \mu\Omega \text{ cm}$ ). In the transition region from the  $\beta$  to  $\alpha$  phase, the resistivity drops precipitously by almost 50%.

Using the same method, we obtained  $\Theta_{SH}^{eff}$  in  $\text{Ta}_{0.25}\text{W}_{0.75}$  with thicknesses from 3.0 to 20.7 nm, as shown in Fig. 3(c). It is noted that  $\Theta_{SH}^{eff}$  is always negative and we present the absolute value  $|\Theta_{SH}^{eff}|$  in Fig. 3(c). When the thickness is increased from 3.0 to 5.3 nm, the  $|\Theta_{SH}^{eff}|$  of  $\beta$ - $\text{Ta}_{0.25}\text{W}_{0.75}$  increases from 0.36 to a peak value of about 0.59. Further increasing the thickness to 7.5 nm lowers the  $|\Theta_{SH}^{eff}|$  to 0.33. When the thickness is beyond 7.5 nm, the  $\alpha$  phase emerges in the structure. This causes the  $|\Theta_{SH}^{eff}|$  to drop to 0.15 in 9.0-nm-thick  $\text{Ta}_{0.25}\text{W}_{0.75}$ , and 0.06 in 20.7-nm-thick  $\text{Ta}_{0.25}\text{W}_{0.75}$ . In comparison, it has been shown that in pure  $\beta$ -W films,  $|\Theta_{SH}^{eff}|$  increases monotonically with increasing thickness up to 18 nm, reaching a nearly saturated value of 0.57 [18,20]. Such thickness dependence can be explained by the change in the spin-diffusion length ( $\lambda_{sf}$ ) relative to the film thickness

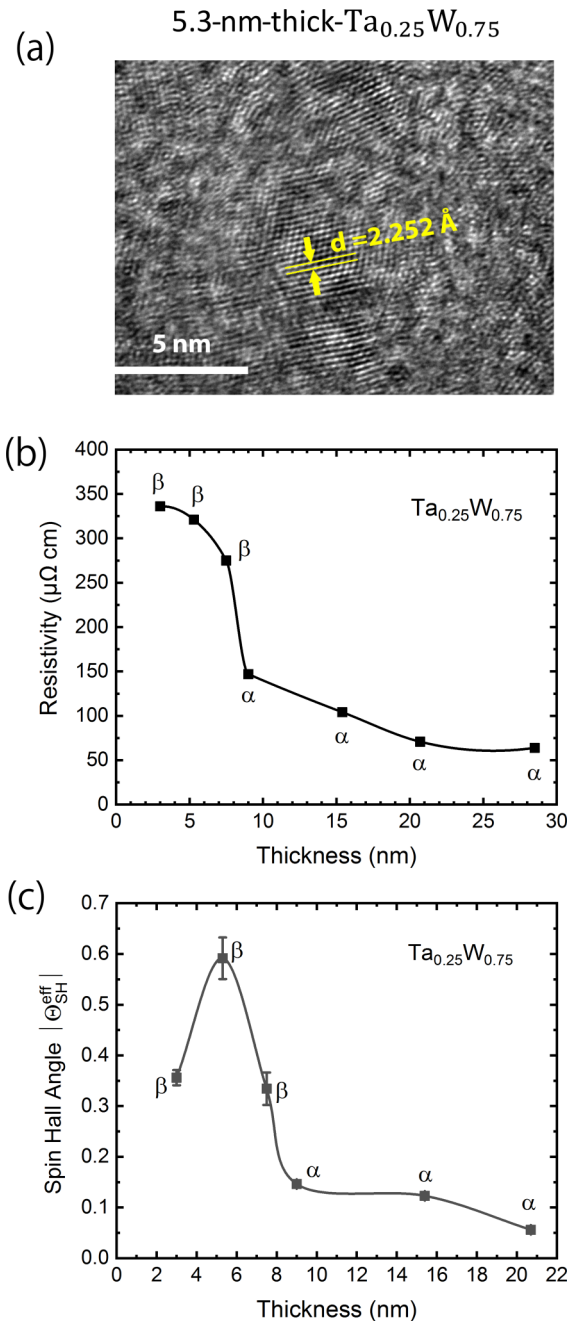


FIG. 3. (a) TEM micrograph of a 5.3-nm-thick  $\text{Ta}_{0.25}\text{W}_{0.75}$  thin film, revealing atomic spacing of  $2.252 \pm 0.024 \text{ \AA}$ . (b) Resistivity vs thickness in  $\text{Ta}_{0.25}\text{W}_{0.75}$ . (c) Spin Hall angle  $|\Theta_{SH}^{eff}|$  vs thickness in  $\text{Ta}_{0.25}\text{W}_{0.75}$ .

[18,20]. The increase in SHA of  $\text{Ta}_{0.25}\text{W}_{0.75}$  from 3.0 to 5.3 nm is possibly due to the same effect as that in pure  $\beta$ -W films. The decrease in SHA from 5.3 nm may be because of its close proximity to the  $\beta$ - to  $\alpha$ -phase transition. Overall, both  $\beta$ - $\text{Ta}_{0.25}\text{W}_{0.75}$  and  $\beta$ -W possess large  $|\Theta_{SH}^{eff}|$  of about 0.6. However,  $\beta$ - $\text{Ta}_{0.25}\text{W}_{0.75}$  requires a thickness of only 5.3 nm *vis-à-vis* 18 nm for  $\beta$ -W. In applications, a thinner film is advantageous as it requires a lower net current to achieve  $J_{sw}$ , and it is easier to deposit a thinner film in mass production.

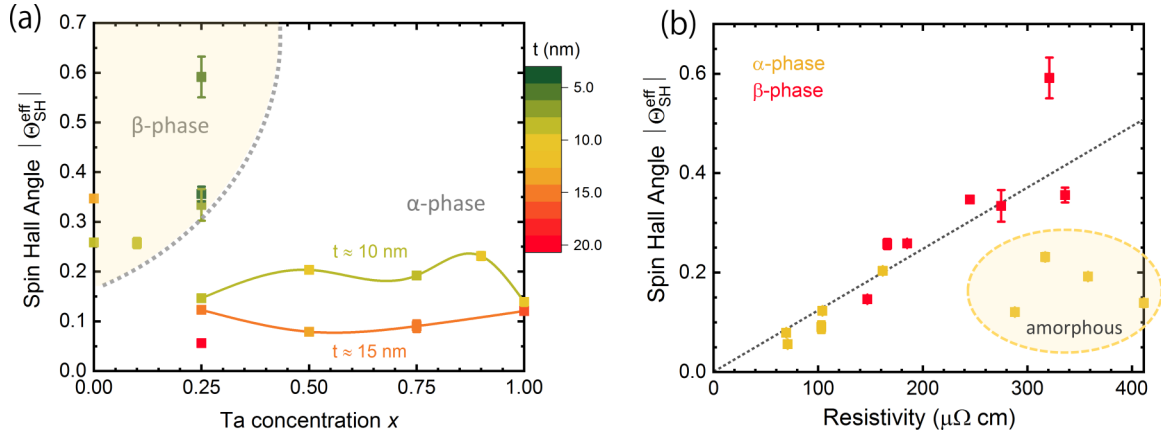


FIG. 4. (a) Spin Hall angles  $|\Theta_{SH}^{eff}|$  of  $\alpha$ - and  $\beta$ - $Ta_xW_{1-x}$  in the full composition range and with various thicknesses. (b) Correlation between spin Hall angle  $|\Theta_{SH}^{eff}|$  and resistivity in  $\alpha$ - and  $\beta$ - $Ta_xW_{1-x}$  alloy systems. The red (yellow) points refer to  $\beta$  phase ( $\alpha$  phase). The outliers in the circle are from amorphous samples with grain sizes smaller than 2.3 nm.

Furthermore, we have measured SHAs of  $\alpha$ - and  $\beta$ - $Ta_xW_{1-x}$  thin films in the full composition range and with various thicknesses, as summarized in Fig. 4(a). Overall, the alloy tends to form a  $\beta$ -phase structure when the film is W rich and thinner, while the stable  $\alpha$  phase occupies a prevalent phase space in Fig. 4(a).  $|\Theta_{SH}^{eff}|$  in  $\beta$ - $Ta_xW_{1-x}$  is larger than that in  $\alpha$ - $Ta_xW_{1-x}$  by two to three times. For pure  $\beta$ -W, our determined  $\Theta_{SH}^{eff}$  values,  $-0.26$  at 8.9 nm and  $-0.35$  at 12.7 nm, are comparable to the previous research results [15,18]. The  $\Theta_{SH}^{eff}$  value for  $\beta$ - $Ta_{0.1}W_{0.9}$  is similar to that for  $\beta$ -W. However, when the Ta concentration reaches 0.25, the  $\Theta_{SH}^{eff}$  value takes a substantial enhancement to  $-0.59$  at the thickness of 5.3 nm, more than doubling the value of  $\beta$ -W at a similar thickness. Figure 4(a) also shows that SHAs of  $\alpha$ -phase alloys, though smaller than those of  $\beta$ -phase alloys, are in fact quite large, in the range of  $-0.06$  to  $-0.23$ . Its SHC is in the range of  $-338$  to  $-1259$  ( $\hbar/2e$ ) (S/cm), which is comparable to the SHC of approximately  $-700$  ( $\hbar/2e$ ) (S/cm) in  $\beta$ -Ta [1,18] and  $590$  ( $\hbar/2e$ ) (S/cm) in Pt [16]. This is contradictory to the common belief that only  $\beta$ -W or  $\beta$ -Ta can exhibit large SHE [3,15,19,20,49]. In addition, we observed that  $|\Theta_{SH}^{eff}|$  decreases with increasing thickness in  $\alpha$ - $Ta_xW_{1-x}$ , which is opposite to the thickness dependence of  $|\Theta_{SH}^{eff}|$  in  $\beta$ -W [18,19].

To reveal mechanisms contributing to the SHE in the  $Ta_xW_{1-x}$ , we explore the relation between SHA and resistivity in both  $\alpha$ - and  $\beta$ - $Ta_xW_{1-x}$  thin films. Analogous to the anomalous Hall effect in FM solids [14,50], the primary cause of SHE is the spin-orbit interaction which favors heavy elements. The origin of SHE could be both intrinsic and extrinsic. The intrinsic mechanism depends on the band structure of a perfect crystal. Extrinsic spin-orbit scattering mechanisms include skew scattering and side jump due to structural disorders and impurities. The skew scattering-induced spin Hall conductivity  $\sigma_{SH}$  is proportional to the electron transport time  $\tau^1$ , while intrinsic or side jump-induced Hall conductivity  $\sigma_{SH}$  is proportional to  $\tau^0$  [14,23]. Correspondingly,  $\Theta_{SH} = \frac{2e}{\hbar} \frac{\sigma_{SH}}{\sigma_0}$ , where  $\sigma_0$  is the sample's conductance, induced by skew scattering is a constant and is independent of sample's resistivity. On the other hand,  $\Theta_{SH}$  induced by the intrinsic mechanism and/or side jump depend linearly on samples' resistivity. In Fig. 4(b),

we observe a linear relationship between  $|\Theta_{SH}^{eff}|$  and resistivity. This provides strong evidence that the intrinsic mechanism and/or side jump are the primary cause of the SHE in both  $\alpha$ - $Ta_xW_{1-x}$  and  $\beta$ - $Ta_xW_{1-x}$ . Due to the existence of impurities and impurity-induced high resistivities, the SHC measured in our experiments are much smaller than the theoretical predicted SHC in  $\beta$ - $Ta_xW_{1-x}$  alloys, although we did observe the enhancement of SHA through alloying.

In Fig. 4(b), we also observe that a few samples' data points are clustered inside the circled region below the linear correlation trend line. These samples are  $\alpha$ - $Ta_xW_{1-x}$  with high resistivities and small grain sizes less than 2.3 nm. Their structures are nearly amorphous, which suppresses the intrinsic contribution to the SHE greatly. It explains why these samples do not follow the linear correlation between SHA and resistivity. It is hard to distinguish contributions of the intrinsic mechanism and side jump to the SHE. However, the large impurity density and moderate spin Hall angles in the samples inside the circled region implies that the intrinsic mechanism contributes to a significant part in the large SHAs observed in other samples.

## V. CONCLUSION

Metastable  $\beta$ -Ta and  $\beta$ -W are archetypes of spin-orbit solids exhibiting SHE. We have carried out a systematic study on the SHE of both the  $\beta$ - and  $\alpha$ - $Ta_xW_{1-x}$  alloy films in the full composition range and with various thicknesses. We have performed structural analysis, magnetic and magnetotransport measurements on all of our samples. Based on the macrospin model, we have measured the effective SHAs of alloys in various compositions and at various thicknesses. We have obtained the largest SHA of  $\Theta_{SH}^{eff} = -0.59$  in a 5.3-nm-thick  $\beta$ - $Ta_{0.25}W_{0.75}$ , which doubles the SHA in  $\beta$ -W [15,20] and is a five times enhancement over the SHA of  $\beta$ -Ta [1,19], at comparable thicknesses. Hence, the effect of alloying on SHE is substantial and beneficial for applications. The critical switching current density on the neighboring  $Co_{40}Fe_{40}B_{20}$  film with perpendicular magnetic anisotropy is found to be on the order of  $10^6$  A/cm<sup>2</sup> with a moderate biasing field. The

small thickness of 5.3 nm makes thin-film deposition easy for device manufacturing, and for reducing the net current required for effective magnetization switching. We have found that  $\alpha$ - $\text{Ta}_x\text{W}_{1-x}$  have smaller SHAs compared to their  $\beta$ -phase counterparts, but they also have much larger SHAs than  $\alpha$ -Ta and  $\alpha$ -W. For example, a 9.7-nm-thick  $\alpha$ - $\text{Ta}_{0.9}\text{W}_{0.1}$  has a SHA of  $-0.23$ . Finally, we have observed a linear correlation between SHA and resistivity in both  $\beta$ - and  $\alpha$ - $\text{Ta}_x\text{W}_{1-x}$  alloy

systems. This is strong evidence that SHE is predominantly caused by the intrinsic mechanism and/or the extrinsic side jump scattering.

#### ACKNOWLEDGMENT

This work was supported by the National Science Foundation (NSF) under Grant No. OMA-1936221.

- 
- [1] L. Liu, C.-F. Pai, Y. Li, H. Tseng, D. Ralph, and R. Buhrman, *Science* **336**, 555 (2012).
- [2] I. M. Miron, K. Garello, G. Gaudin, P.-J. Zermatten, M. V. Costache, S. Auffret, S. Bandiera, B. Rodmacq, A. Schuhl, and P. Gambardella, *Nature (London)* **476**, 189 (2011).
- [3] L. Liu, O. J. Lee, T. J. Gudmundsen, D. C. Ralph, and R. A. Buhrman, *Phys. Rev. Lett.* **109**, 096602 (2012).
- [4] W. Chen, L. Qian, and G. Xiao, *Sci. Rep.* **8**, 8144 (2018).
- [5] X. Z. Chen, R. Zarzuela, J. Zhang, C. Song, X. F. Zhou, G. Y. Shi, F. Li, H. A. Zhou, W. J. Jiang, F. Pan, and Y. Tserkovnyak, *Phys. Rev. Lett.* **120**, 207204 (2018).
- [6] T. Moriyama, W. Zhou, T. Seki, K. Takahashi, and T. Ono, *Phys. Rev. Lett.* **121**, 167202 (2018).
- [7] L. Baldrati, O. Gomonay, A. Ross, M. Filianina, R. Lebrun, R. Ramos, C. Leveille, F. Fuhrmann, T. R. Forrest, F. Maccherozzi, S. Valencia, F. Kronast, E. Saitoh, J. Sinova, and M. Kläui, *Phys. Rev. Lett.* **123**, 177201 (2019).
- [8] J. Li, P. Ndai, A. Goel, S. Salahuddin, and K. Roy, *IEEE Trans. Very Large Scale Integr. VLSI Syst.* **18**, 1710 (2009).
- [9] Y. Huai, *AAPPS Bull.* **18**, 33 (2008).
- [10] M. Cubukcu, O. Boulle, M. Drouard, K. Garello, C. Onur Avci, I. Mihai Miron, J. Langer, B. Ocker, P. Gambardella, and G. Gaudin, *Appl. Phys. Lett.* **104**, 042406 (2014).
- [11] T. Jungwirth, X. Marti, P. Wadley, and J. Wunderlich, *Nat. Nanotechnol.* **11**, 231 (2016).
- [12] K. Wang, L. Qian, S.-C. Ying, G. Xiao, and X. Wu, *Nanoscale* **11**, 6952 (2019).
- [13] J. E. Hirsch, *Phys. Rev. Lett.* **83**, 1834 (1999).
- [14] J. Sinova, S. O. Valenzuela, J. Wunderlich, C. H. Back, and T. Jungwirth, *Rev. Mod. Phys.* **87**, 1213 (2015).
- [15] C.-F. Pai, L. Liu, Y. Li, H.-W. Tseng, D. C. Ralph, and R. A. Buhrman, *Appl. Phys. Lett.* **101**, 122404 (2012).
- [16] M.-H. Nguyen, D. C. Ralph, and R. A. Buhrman, *Phys. Rev. Lett.* **116**, 126601 (2016).
- [17] W. Zhang, W. Han, X. Jiang, S.-H. Yang, and S. S. P. Parkin, *Nat. Phys.* **11**, 496 (2015).
- [18] Q. Hao and G. Xiao, *Phys. Rev. Appl.* **3**, 034009 (2015).
- [19] Q. Hao and G. Xiao, *Phys. Rev. B* **91**, 224413 (2015).
- [20] W. Chen, G. Xiao, Q. Zhang, and X. Zhang, *Phys. Rev. B* **98**, 134411 (2018).
- [21] D. Qu, S. Y. Huang, G. Y. Guo, and C. L. Chien, *Phys. Rev. B* **97**, 024402 (2018).
- [22] M. Obstbaum, M. Decker, A. K. Greitner, M. Haertinger, T. N. G. Meier, M. Kronseder, K. Chadova, S. Wimmer, D. Ködderitzsch, and H. Ebert, and C. H. Back, *Phys. Rev. Lett.* **117**, 167204 (2016).
- [23] P. Laczkowski, Y. Fu, H. Yang, J.-C. Rojas-Sánchez, P. Noël, V. T. Pham, G. Zahnd, C. Deranlot, S. Collin, C. Bouard *et al.*, *Phys. Rev. B* **96**, 140405(R) (2017).
- [24] P. Laczkowski, J.-C. Rojas-Sánchez, W. Savero-Torres, H. Jaffrès, N. Reyren, C. Deranlot, L. Notin, C. Beigné, A. Marty, and J.-P. Attané, *Appl. Phys. Lett.* **104**, 142403 (2014).
- [25] B. Gu, I. Sugai, T. Ziman, G. Y. Guo, N. Nagaosa, T. Seki, K. Takahashi, and S. Maekawa, *Phys. Rev. Lett.* **105**, 216401 (2010).
- [26] R. Ramaswamy, Y. Wang, M. Elyasi, M. Motapothula, T. Venkatesan, X. Qiu, and H. Yang, *Phys. Rev. Appl.* **8**, 024034 (2017).
- [27] L. Zhu, D. C. Ralph, and R. A. Buhrman, *Phys. Rev. Appl.* **10**, 031001 (2018).
- [28] L. K. Zou, S. H. Wang, Y. Zhang, J. R. Sun, J. W. Cai, and S. S. Kang, *Phys. Rev. B* **93**, 014422 (2016).
- [29] Q. Hao, W. Chen, and G. Xiao, *Appl. Phys. Lett.* **106**, 182403 (2015).
- [30] M. H. Read and C. Altman, *Appl. Phys. Lett.* **7**, 51 (1965).
- [31] M. Cecot, Ł. Karwacki, W. Skowroński, J. Kanak, J. Wrona, A. Żywczak, L. Yao, S. van Dijken, J. Barnaś, and T. Stobiecki, *Sci. Rep.* **7**, 968 (2017).
- [32] X. Sui, C. Wang, J. Kim, J. Wang, S. H. Rhim, W. Duan, and N. Kioussis, *Phys. Rev. B* **96**, 241105(R) (2017).
- [33] E. Derunova, Y. Sun, C. Felser, S. Parkin, B. Yan, and M. Ali, *Sci. Adv.* **5**, eaav8575 (2019).
- [34] H. X. Yang, M. Chshiev, B. Dieny, J. H. Lee, A. Manchon, and K. H. Shin, *Phys. Rev. B* **84**, 054401 (2011).
- [35] B. Dieny and M. Chshiev, *Rev. Mod. Phys.* **89**, 025008 (2017).
- [36] P. Petroff, T. T. Sheng, A. K. Sinha, G. A. Rozgonyi, and F. B. Alexander, *J. Appl. Phys.* **44**, 2545 (1973).
- [37] I. A. Weerasekera, S. I. Shah, D. V. Baxter, and K. M. Unruh, *Appl. Phys. Lett.* **64**, 3231 (1994).
- [38] S. Gates-Rector and T. Blanton, *Powder Diffraction* **34**, 352 (2019).
- [39] A. Patterson, *Phys. Rev.* **56**, 978 (1939).
- [40] A. T. D'Agostino, *Anal. Chim. Acta* **262**, 269 (1992).
- [41] A. F. Mayadas and M. Shatzkes, *Phys. Rev. B* **1**, 1382 (1970).
- [42] T. Sun, B. Yao, A. P. Warren, K. Barmak, M. F. Toney, R. E. Peale, and K. R. Coffey, *Phys. Rev. B* **79**, 041402(R) (2009).
- [43] K. Wang, L. Qian, W. Chen, S.-C. Ying, G. Xiao, and X. Wu, *Phys. Rev. B* **99**, 184410 (2019).
- [44] M. Gabor, T. Petrisor Jr., R. Mos, A. Mesáros, M. Nasui, M. Belmeguenai, F. Zighem, and C. Tiusan, *J. Phys. D: Appl. Phys.* **49**, 365003 (2016).

- [45] J. Cao, Y. Chen, T. Jin, W. Gan, Y. Wang, Y. Zheng, H. Lv, S. Cardoso, D. Wei, and W. S. Lew, *Sci. Rep.* **8**, 1 (2018).
- [46] S. Li, S. Goolaup, J. Kwon, F. Luo, W. Gan, and W. S. Lew, *Sci. Rep.* **7**, 1 (2017).
- [47] Y. Zhang, X. Zhang, N. Vernier, Z. Zhang, G. Agnus, J.-R. Coudevylle, X. Lin, Y. Zhang, Y.-G. Zhang, W. Zhao, and D. Ravelosona, *Phys. Rev. Appl.* **9**, 064027 (2018).
- [48] K.-S. Ryu, L. Thomas, S.-H. Yang, and S. Parkin, *Nat. Nanotechnol.* **8**, 527 (2013).
- [49] M. Morota, Y. Niimi, K. Ohnishi, D. H. Wei, T. Tanaka, H. Kontani, T. Kimura, and Y. Otani, *Phys. Rev. B* **83**, 174405 (2011).
- [50] N. Nagaosa, J. Sinova, S. Onoda, A. H. MacDonald, and N. P. Ong, *Rev. Mod. Phys.* **82**, 1539 (2010).